

# Nearly Complete Charge–Spin Conversion via Strain-Eliminated Fermi Pockets in a $d$ -Wave Altermagnet

Wancheng Zhang <sup>1</sup>, Zhenhua Zhang <sup>2,\*</sup>, Rui Xiong <sup>3</sup> and Zhihong Lu <sup>2,†</sup>

<sup>1</sup>*School of Electrical and Electronic Information Engineering, Hubei Polytechnic University, Huangshi 435003, People's Republic of China*

<sup>2</sup>*School of Materials Science and Engineering, Wuhan University of Science and Technology, Wuhan 430081, People's Republic of China*

<sup>3</sup>*Key Laboratory of Artificial Micro- and Nano-structures of Ministry of Education, School of Physics and Technology, Wuhan University, Wuhan 430072, People's Republic of China*

(Dated: April 24, 2026)

The room-temperature altermagnet  $KV_2Se_2O$  possesses nearly orthogonal flat Fermi surfaces, which in an idealized  $d$ -wave limit enable complete spin-channel separation and a theoretical charge-to-spin conversion efficiency (CSE) of 100%. Realistic samples, however, host residual elliptical Fermi pockets that enhance charge conductivity while suppressing spin conductivity, drastically reducing the CSE. Here we show that in-plane equibiaxial tensile strain systematically eliminates these parasitic pockets, restoring the flat-band geometry. Our first-principles calculations reveal that the CSE increases monotonically with strain, reaching a record value of approximately 96% at 4% strain. An effective tight-binding model fitted to the computed band structure accurately captures the evolution of the Fermi surface and confirms that the suppression of the pockets—governed by reduced next-nearest-neighbor hoppings—is the dominant mechanism for the strain-enhanced CSE. We further identify an unconventional out-of-plane spin current that emerges under tilted electric fields and achieves a CSE of nearly 55% at optimal orientations, offering a promising pathway for field-free perpendicular magnetization switching. Our work establishes strain engineering as a practical route to approach the ultimate conversion limit in altermagnets and provides a design principle for high-efficiency spintronic devices.

*Introduction*—Altermagnetism represents a newly recognized class of collinear magnetic order that combines the vanishing net magnetization of an antiferromagnet with a momentum-dependent spin splitting reminiscent of a ferromagnet [1–8]. In contrast to conventional antiferromagnets, where opposite-spin sublattices are related by a translation or inversion, altermagnets require a proper rotation or mirror operation to connect the sublattices, giving rise to a nonrelativistic  $d$ -,  $g$ -, or  $i$ -wave spin splitting even in the absence of spin-orbit coupling (SOC) [1, 9, 10]. This unique symmetry enables the generation of time-reversal-odd ( $\mathcal{T}$ -odd) spin currents with efficiencies that can far exceed those of conventional spin Hall materials, opening a transformative avenue for next-generation spintronic memory and logic devices [11–13].

A particularly compelling limit arises in  $d$ -wave altermagnets possessing two mutually orthogonal flat Fermi surfaces with opposite spin polarizations [14]. As captured by a minimal two-band model, extreme spin-splitting anisotropy ( $a/b \rightarrow 0$  or  $\infty$ ) yields perfectly flat, orthogonal Fermi sheets, corresponding to complete spin-channel separation in momentum space. Under a longitudinal electric field along a  $\langle 100 \rangle$  direction, a fully spin-polarized current flows; under a field along a  $\langle 110 \rangle$  direction, a pure transverse spin current emerges with a magnitude equal to the total charge current. In this ideal

configuration, the charge-to-spin conversion efficiency (CSE) reaches its theoretical upper limit of 100% [14].

Recent experiments have identified the layered vanadium selenide oxide  $KV_2Se_2O$  as a rare metallic room-temperature  $d$ -wave altermagnet [15]. The opposite-spin sublattices are related by the  $[C_2||C_{4z}]$  spin-space symmetry [1, 2, 9], which lifts Kramers degeneracy without spin-orbit coupling and produces a giant momentum-dependent spin splitting of  $\sim 1.6$  eV at the  $X$  and  $Y$  points [10, 15]. First-principles calculations reveal that the pristine compound already exhibits a remarkable CSE of  $\sim 78\%$  at the charge neutrality point—nearly double that of the benchmark altermagnet  $RuO_2$ —and can approach 98% under modest electron doping, making it the most efficient  $\mathcal{T}$ -odd spin-current generator reported to date [14].

Despite this record performance, pristine  $KV_2Se_2O$  falls short of the ideal 100% limit due to the presence of residual elliptical Fermi pockets near the  $X$  and  $Y$  points. These pockets, inherited from slight warping of the otherwise flat bands, act as parasitic conduction channels: they enhance the charge conductivity while contributing oppositely to the spin conductivity, thereby diluting the CSE [14]. A natural strategy to eliminate these detrimental pockets and recover the ideal flat-band geometry is strain engineering, which has already proven effective in tuning altermagnetic properties in related materials such as  $RuO_2$ ,  $MnTe$ ,  $CrSb$  and  $OsO_2$  [16–19].

In this Letter, we demonstrate that in-plane equibiaxial tensile strain provides a practical and highly effective means to restore the perfect orthogonal flat Fermi surfaces in  $KV_2Se_2O$ .

\* Contact author: zzhua@wust.edu.cn

† Contact author: zludavid@live.com

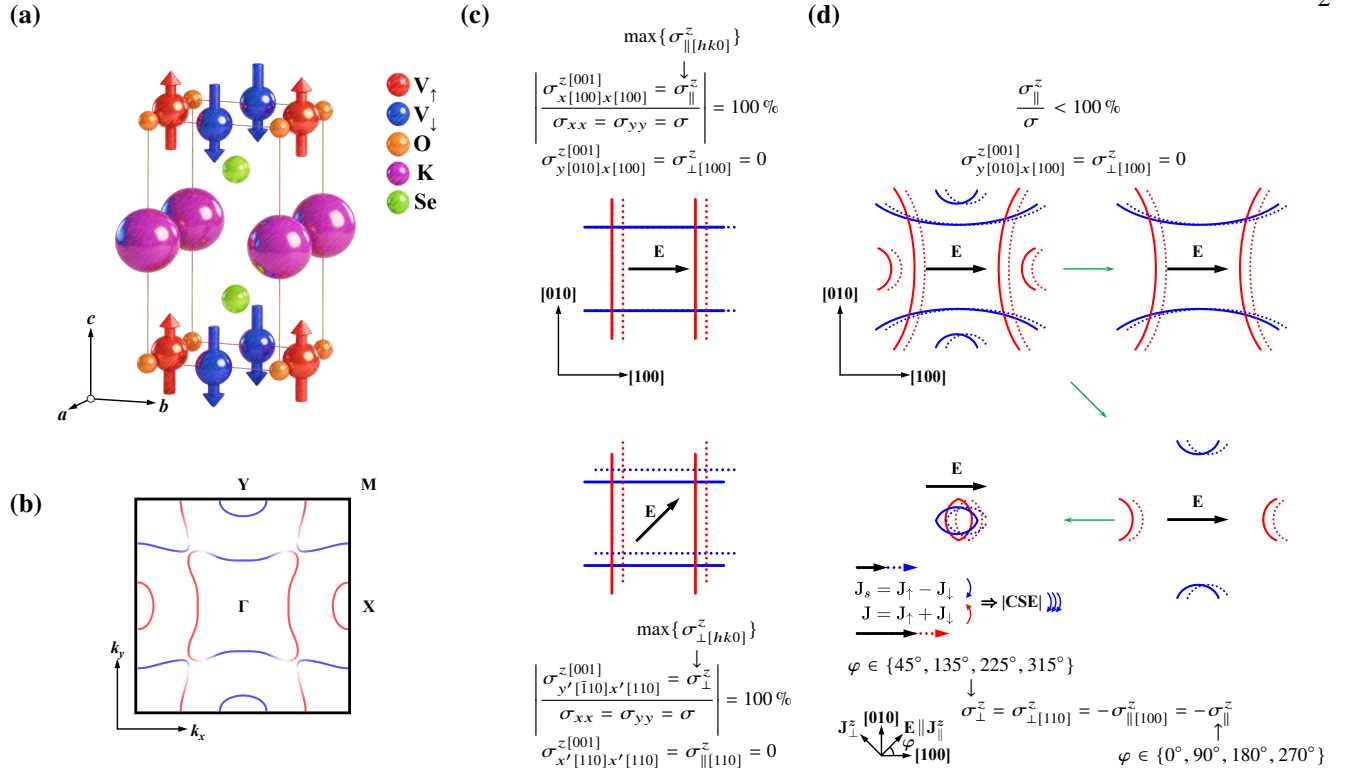


FIG. 1. Atomic structure, spin-resolved Fermi surface, and schematic of spin-current generation in KV<sub>2</sub>Se<sub>2</sub>O. Red and blue denote opposite spin orientations (up and down, respectively). (a) Crystal structure and spin configuration of KV<sub>2</sub>Se<sub>2</sub>O. (b) Spin-resolved Fermi surface in the  $k_z = 0$  plane obtained from first-principles calculations. (c) Idealized spin-current generation. The spin-up and spin-down Fermi surfaces are perfectly orthogonal flat sheets. When an electric field  $\mathbf{E}$  is applied along a  $\langle 100 \rangle$  equivalent direction, a pure longitudinal spin-polarized current  $\mathbf{J}_{\parallel}^z = \mathbf{J}_{\uparrow}$  is generated, quantified by the spin conductivity  $\sigma_{\parallel}^z$ . When  $\mathbf{E}$  is applied along a  $\langle 110 \rangle$  equivalent direction, a pure transverse spin current  $\mathbf{J}_{\perp}^z = \mathbf{J}_{\uparrow} - \mathbf{J}_{\downarrow}$  emerges. Owing to the orthogonality of the flat bands, its magnitude satisfies  $|\mathbf{J}_{\perp}^z| = |\mathbf{J}| = |\mathbf{J}_{\uparrow} + \mathbf{J}_{\downarrow}|$ , and the corresponding spin conductivity is denoted  $\sigma_{\perp}^z$ . In this ideal limit, the maximum charge–spin conversion efficiency reaches  $|\text{CSE}|_{\text{max}} = \sigma_{\perp}^z / \sigma = \sigma_{\perp}^z / \sigma \equiv 100\%$ , where  $\sigma$  is the charge conductivity. (d) Realistic spin-current generation illustrated for  $\mathbf{E} \parallel [001]$ . Residual Fermi pockets at the X and Y points (lower left inset, analogous to the case of RuO<sub>2</sub>) suppress the spin conductivity while enhancing the charge conductivity, drastically reducing the CSE. Additionally, the slight warping of the energy bands further degrades the CSE relative to the perfectly orthogonal flat-band case, preventing the system from attaining the ideal 100% efficiency.

Our first-principles calculations (based on density functional theory plus Wannier interpolation; hereafter referred to as DFT calculations for brevity) [20] show that the in-plane  $|\text{CSE}|$  increases monotonically with strain, reaching a record value of  $\sim 96\%$  at 4% strain, before slightly declining at larger deformations due to incipient Fermi-surface bending. Furthermore, we uncover an unconventional out-of-plane spin current that emerges when the electric field is tilted away from high-symmetry axes. This out-of-plane component achieves a maximum  $|\text{CSE}_{\uparrow}|$  of nearly 55% at 4% strain and at specific field orientations, offering a promising pathway for field-free perpendicular magnetization switching. Our findings establish strain engineering as a viable route to approach the ultimate CSE limit in altermagnets and highlight KV<sub>2</sub>Se<sub>2</sub>O as a premier platform for high-efficiency spintronic devices.

**Results and discussion**—KV<sub>2</sub>Se<sub>2</sub>O crystallizes in the tetragonal  $P4/mmm$  space group, with spin-up and spin-down V atoms arranged within the same atomic plane. The opposite-

spin sublattices are related by the  $[C_2 || C_{4z}]$  symmetry operation, as illustrated in Fig. 1(a). This unique magnetic configuration endows the material with pronounced crystalline and magnetic anisotropy, enabling strong directional modulation of spin-dependent charge transport. The spin-resolved Fermi surface in the  $k_z = 0$  plane, presented in Fig. 1(b), directly reflects this anisotropic electronic structure: it exhibits the characteristic  $d$ -wave altermagnetic anisotropy [1, 2], wherein spin-up and spin-down states are predominantly orthogonal yet retain small residual pockets near the X and Y points that break the perfect flat-band limit.

The idealized spin-current generation mechanism is illustrated in Fig. 1(c): in the perfect  $d$ -wave altermagnetic limit, the spin-up and spin-down Fermi surfaces form mutually orthogonal flat sheets. An electric field along  $\langle 100 \rangle$  drives a purely longitudinal spin-polarized current, while a field along  $\langle 110 \rangle$  generates a pure transverse spin current whose magnitude equals the total charge current, yielding a theoretical

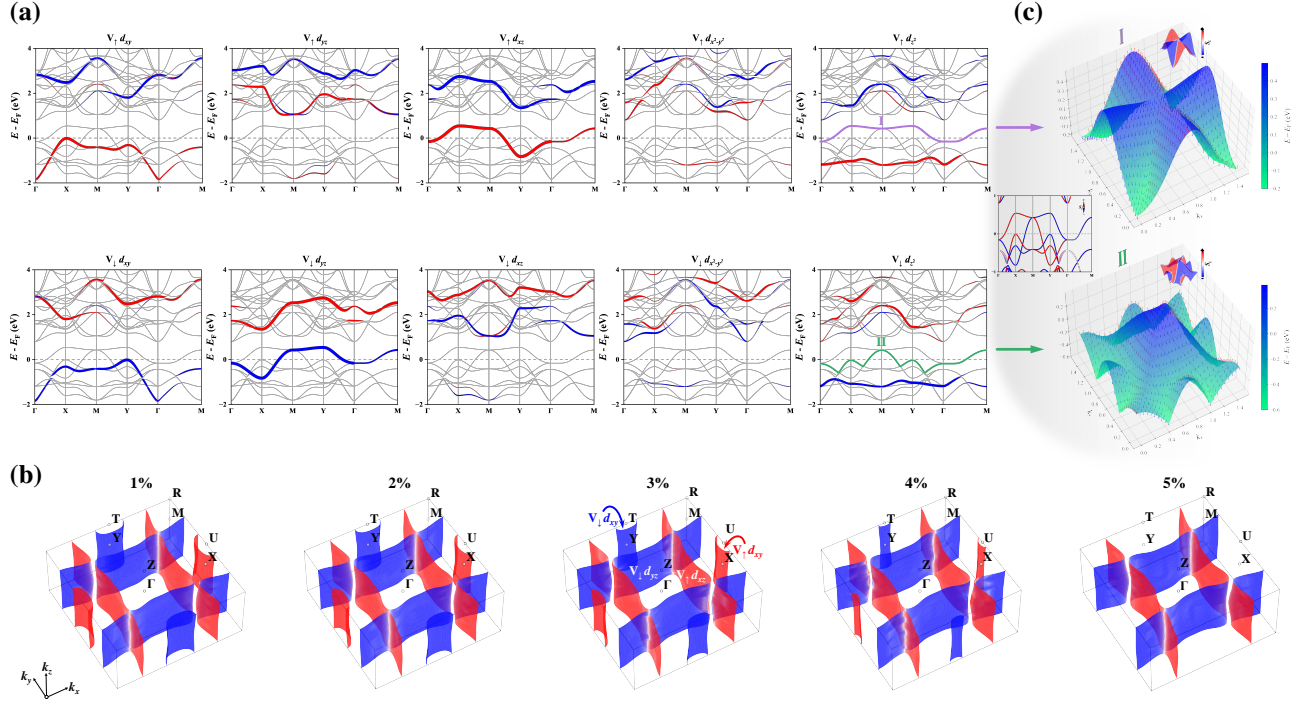


FIG. 2. Band structure and Fermi surface of  $KV_2Se_2O$  under equibiaxial tensile strain. (a) Calculated orbital- and spin-resolved band structures along high-symmetry lines at 4% strain. Red and blue dots represent spin-up and spin-down bands, respectively. The size of the dots scales with the projection weight of the V  $d_{xy}$ ,  $d_{yz}$ ,  $d_{xz}$ ,  $d_{x^2-y^2}$ , and  $d_{z^2}$  orbitals. (b) Spin-resolved three-dimensional Fermi surfaces at 1%, 2%, 3%, 4%, and 5% strain. (c) Spin texture of the two bands crossing the Fermi level [marked in purple and green in (a)] at 4% strain. The arrows indicate the spin orientation, with red (blue) denoting positive (negative) out-of-plane spin component  $S_z$ . The surface color encodes the band energy. The inset shows the corresponding three-dimensional bands colored by  $S_z$ . Throughout the figure, red and blue represent spin-up and spin-down states, respectively.

[CSE] of 100%. In reality, as depicted in Fig. 1(d), residual elliptical pockets near X and Y act as parasitic conduction channels that enhance the charge conductivity while contributing oppositely to the spin conductivity, thereby reducing the CSE far below the ideal limit.

Figure 2(a) displays the orbital- and spin-resolved band structure of  $KV_2Se_2O$  at 4% equibiaxial tensile strain (see band structures at all strain in Supplemental Material [20]). The overall band dispersion and the pronounced spin splitting near the X and Y points are in excellent agreement with the results reported by Jiang *et al.* [15]. From Figs. 2(a) and 2(b) it is evident that the mutually orthogonal flat bands—the primary source of the large CSE—are predominantly derived from the spin-up V  $d_{xz}$  and spin-down V  $d_{yz}$  orbitals, oriented nearly along the  $k_y$  and  $k_x$  directions, respectively. The elliptical pockets emerging near X and Y, on the other hand, originate from the spin-up and spin-down V  $d_{xy}$  orbitals. As illustrated schematically in Fig. 1(d), these pockets act as parasitic conduction channels that suppress the spin conductivity and therefore limit the overall CSE.

The distinctive  $d$ -wave flat Fermi surface of  $KV_2Se_2O$  and its strain-enhanced charge-to-spin conversion can be captured by an effective two-orbital tight-binding model (four bands in

total). In the absence of spin-orbit coupling, the Hamiltonian decouples into spin-up and spin-down sectors related by the altermagnetic  $[C_2||C_{4z}]$  symmetry. For each spin projection, we adopt a  $2 \times 2$  low-energy basis that phenomenologically describes the flat sheet (derived from the  $d_{xz}/d_{yz}$  orbitals) and the elliptical pocket (originating from the  $d_{xy}$  orbital). Fitting to the DFT band structure yields the hopping parameters listed in the Supplemental Material [20]. The model naturally reproduces the orthogonal flat Fermi segments along  $k_x$  and  $k_y$ , as well as the isolated pockets at X and Y, providing a transparent framework for analyzing the strain-driven evolution of the CSE.

The spin texture of the two bands crossing the Fermi level at 4% strain is shown in Fig. 2(c). The arrows, colored by the out-of-plane spin component  $S_z$ , point predominantly along the  $z$  direction, indicating that the spin polarization is almost entirely out-of-plane. A clear  $d$ -wave pattern emerges in the sign distribution of  $S_z$ : positive and negative values are separated by the nodal lines  $k_x = \pm k_y$ , across which the spin polarization abruptly reverses [21, 22]. Along a fixed band index, this reversal is particularly sharp in the vicinity of the elliptical pockets at X and Y, where the DFT eigenvalues switch between the spin-up and spin-down branches of the  $d_{x^2-y^2}$ -wave spin split-

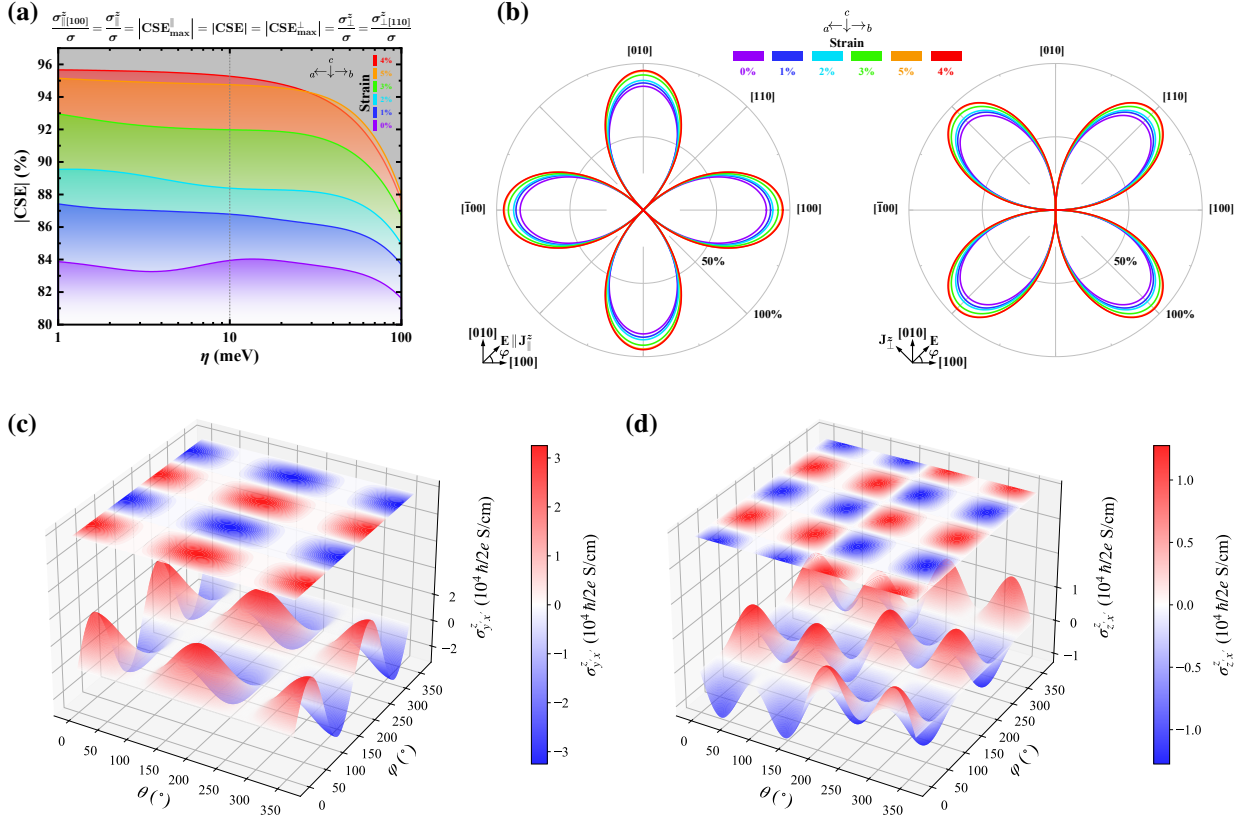


FIG. 3. Strain and angular dependence of the charge-to-spin conversion efficiency (CSE) and spin conductivities in  $\text{KV}_2\text{Se}_2\text{O}$  evaluated with a broadening parameter  $\eta = 10$  meV. (a) Strain-dependent CSE as a function of  $\eta$ . (b) Polar plots of the longitudinal (left) and transverse (right) CSE under an in-plane rotating electric field at various strain levels. The fourfold symmetry and the relation  $\text{CSE}_\perp(\varphi = 45^\circ) = -\text{CSE}_\parallel(\varphi = 0^\circ)$  are direct consequences of the  $d$ -wave altermagnetic order. (c) Full-angle dependence of the transverse spin conductivity  $\sigma_{y'x'z'}^z$  at 0% strain, shown as a 3D surface combined with a top-view contour projection. (d) Corresponding out-of-plane spin conductivity  $\sigma_{z'x'z'}^z$  displayed in the same 3D-plus-contour representation.

ting [23]. Within the effective tight-binding model, the spin splitting is dominated by the  $(\cos k_x - \cos k_y)$  term, which vanishes along the diagonals and attains opposite signs on either side of the pockets (a detailed symmetry analysis is provided in the Supplemental Material [20]). The sign change along the band index therefore maps directly onto the nodal structure of the  $d$ -wave order, confirming that the pocket regions act as momentum-space domain boundaries where the spin character of the highest valence bands is exchanged. This observation further corroborates the altermagnetic nature of  $\text{KV}_2\text{Se}_2\text{O}$  and highlights the intimate connection between Fermi surface topology and spin-dependent transport.

The altermagnetic symmetry not only dictates the Fermi surface topology but also governs the angular dependence of the spin currents. To quantify this, we compute the longitudinal and transverse CSEs as the electric field rotates within the  $xy$  plane. As shown in Fig. 3(b), the longitudinal CSE exhibits a fourfold symmetric pattern with maxima along  $\langle 100 \rangle$  directions, while the transverse CSE peaks along  $\langle 110 \rangle$  and vanishes along  $\langle 100 \rangle$ , consistent with the  $d$ -wave character of the

spin splitting. The two satisfy the exact relation  $|\text{CSE}_\perp|(\varphi = 45^\circ) = |\text{CSE}_\parallel|(\varphi = 0^\circ)$ , inherited from the  $[C_2||C_{4z}]$  symmetry.

When the electric field is allowed to tilt out of the  $ab$  plane, an unconventional out-of-plane spin current emerges. Figs. 3(c) and 3(d) display the full angular dependence of the transverse in-plane and out-of-plane spin conductivities over the entire solid angle  $(\theta, \varphi)$ . The in-plane transverse component dominates near the equatorial plane ( $\theta = 90^\circ$ ) and exhibits the same fourfold oscillation as in the strictly two-dimensional case. For convenience, we denote the maximum in-plane (longitudinal/transverse) spin conductivity by  $\sigma_\pm^s$  and the corresponding maximum charge-to-spin conversion efficiency by CSE. In contrast, the out-of-plane spin conductivity  $\sigma_{z'x'z'}^z$  vanishes identically within cones centered on the  $c$  axis ( $\theta \approx 90^\circ$  and  $270^\circ$ , half-angle  $\sim 3^\circ$ ), and reaches maximal magnitude (hereafter denoted  $\sigma_{\hat{n}}^{\hat{n}}$ , with  $\hat{n}$  being the Néel vector direction) when the field is tilted by  $\sim 35^\circ$  toward  $\langle 100 \rangle$  or  $\langle 010 \rangle$ , corresponding closely to the  $\langle 101 \rangle$  and  $\langle 011 \rangle$  crystal directions. The symmetry-enforced relation  $\sigma_{\hat{n}}^{\hat{n}}(\varphi + 90^\circ) =$

$-\sigma_{\uparrow}^{\hat{n}}(\varphi)$  is strictly observed for the signed conductivity, confirming the  $[C_2 \parallel C_{4z}]$  altermagnetic order. The corresponding maximum out-of-plane CSE is denoted  $\text{CSE}_{\uparrow}^{\hat{n}}$ . A complete list of extrema, their crystallographic assignments, and a detailed discussion of the rotation formalism are provided in the Supplemental Material [20].

TABLE I. Strain dependence of the in-plane spin conductivity  $|\sigma_{\uparrow}^s| = |\sigma_{\downarrow}^s| = |\sigma_{\perp}^s|$ , the out-of-plane spin conductivity  $|\sigma_{\uparrow}^{\hat{n}}|$ , and the corresponding charge-to-spin conversion efficiencies  $|\text{CSE}|$  (in-plane) and  $|\text{CSE}_{\uparrow}|$  (out-of-plane) for  $\text{KV}_2\text{Se}_2\text{O}$ . All spin conductivities are in units of  $(\hbar/2e)$  S/cm.

Strain (%)	$ \sigma_{\uparrow}^s $	$ \sigma_{\uparrow}^{\hat{n}} $	$ \text{CSE} $ ( $ \text{CSE}_{\uparrow} $ ) (%)
0	$3.17 \times 10^4$	$1.28 \times 10^4$	83.95 (48.56)
1	$3.09 \times 10^4$	$1.20 \times 10^4$	86.79 (49.67)
2	$2.71 \times 10^4$	$1.10 \times 10^4$	88.39 (50.51)
3	$2.58 \times 10^4$	$1.02 \times 10^4$	91.98 (52.64)
4	$2.58 \times 10^4$	$1.01 \times 10^4$	95.26 (54.34)
5	$2.46 \times 10^4$	$0.96 \times 10^4$	94.75 (54.10)

Table I summarizes the strain evolution of the in-plane and out-of-plane spin conductivities as well as the corresponding CSEs. With increasing tensile strain, the in-plane spin conductivity  $|\sigma_{\uparrow}^s|$  decreases monotonically from  $3.17 \times 10^4$  to  $2.46 \times 10^4$   $(\hbar/2e)$  S/cm, while the in-plane  $|\text{CSE}|$  rises from  $\sim 84\%$  (the slight difference from the value reported by Lai *et al.* [14] originates from the use of Hubbard  $U$  [15, 20, 24, 25] corrections and different pseudopotentials) to a peak value of 95.26% at 4% strain. The out-of-plane spin conductivity  $|\sigma_{\uparrow}^{\hat{n}}|$  exhibits a similar downward trend, dropping from  $1.28 \times 10^4$  to  $0.96 \times 10^4$   $(\hbar/2e)$  S/cm, yet its associated conversion efficiency  $|\text{CSE}_{\uparrow}|$  increases from 48.56% to 54.34% over the same strain range. This concurrent enhancement of both in-plane and out-of-plane CSEs further supports the conclusion that the elimination of parasitic Fermi pockets under strain universally improves the charge-to-spin conversion performance.

Table II lists the optimal crystallographic orientations that maximize the  $\text{CSE}_{\text{or}}^{\hat{n}}$  under different strain levels. Two representative directions are identified: (011) and (111), both of which yield identical CSE values at each strain owing to symmetry. Interestingly, while the in-plane  $|\text{CSE}|$  peaks at 4% strain and slightly declines at 5% (see Table I), the out-of-plane CSE continues to increase up to 5%, reaching 50.01%. This distinct behavior stems from the fact that the out-of-plane spin current is more sensitive to the residual band curvature induced by the parasitic pockets than the in-plane components. As strain increases, the pockets shrink and the Fermi surface becomes flatter, but the out-of-plane response requires a slightly larger deformation to fully saturate. The monotonic rise of

$\text{CSE}_{\text{or}}^{\hat{n}}$  up to 5% thus indicates that the destructive interference among the rotated  $d$ -wave tensor elements is progressively suppressed, allowing the vertical spin current to reach its maximum efficiency at a higher strain than the in-plane counterpart.

TABLE II. Strain-dependent optimal orientations and the corresponding  $\text{CSE}_{\text{or}}^{\hat{n}}$  in  $\text{KV}_2\text{Se}_2\text{O}$ . For the (011) orientation, the new  $x'$  axis (electric-field direction) is  $[01\bar{1}]$  and the new  $y'$  axis is  $[\bar{1}00]$ ; for (111),  $x' = [0\bar{1}1]$  and  $y' = [2\bar{1}1]$ . The angles  $\theta$  and  $\varphi$  define the direction of  $\mathbf{E}$  in the original crystal frame.

Strain (%)	Orientation	$\theta$ ( $^\circ$ )	$\varphi$ ( $^\circ$ )	$\text{CSE}_{\text{or}}^{\hat{n}}$ (%)
0	(011)	151.98	90.00	39.74
	(111)	28.02	270.00	39.74
1	(011)	150.75	90.00	41.88
	(111)	29.25	270.00	41.88
2	(011)	150.27	90.00	44.02
	(111)	29.73	270.00	44.02
3	(011)	149.44	90.00	47.14
	(111)	30.56	270.00	47.14
4	(011)	148.64	90.00	48.83
	(111)	31.36	270.00	48.83
5	(011)	147.86	90.00	50.01
	(111)	32.14	270.00	50.01

To establish a direct link between the microscopic hopping parameters and the strain-enhanced CSE, we employ the effective tight-binding model fitted to the pristine DFT bands (see Supplemental Material [20] for the full Hamiltonian). Fig. 4(a) displays the evolution of the spin-resolved Fermi surface when the next-nearest-neighbor (NNN) [26, 27] hopping terms responsible for the elliptical pockets—i.e., those proportional to  $\cos k_x \cos k_y$ ,  $\cos 2k_x$ , and  $\cos 2k_y$  in the Hamiltonian—are uniformly scaled by a factor ranging from 1.00 (pristine) to 0.80 in steps of 0.04. This global suppression mimics the reduction of longer-range hoppings under in-plane equibiaxial tensile strain. As the scaling factor decreases, the elliptical pockets at  $X$  and  $Y$  gradually shrink and ultimately vanish, leaving only the orthogonal flat sheets characteristic of the ideal  $d$ -wave altermagnetic limit.

Fig. 4(b) shows the corresponding CSE computed from the Kubo formula with a constant broadening  $\eta = 10$  meV, alongside the CSE values obtained from explicit DFT strain calculations. The model CSE rises monotonically from  $\sim 82\%$  to  $\sim 90\%$ , closely following the DFT trend and confirming that pocket elimination is the dominant mechanism for the strain-induced enhancement.

The origin of this enhancement is revealed in Fig. 4(c), where we plot the normalized charge conductivity  $\sigma$  and spin conductivity  $\sigma^s$ . Both conductivities decrease as the pockets are suppressed, but  $\sigma$  drops at a markedly faster rate. This

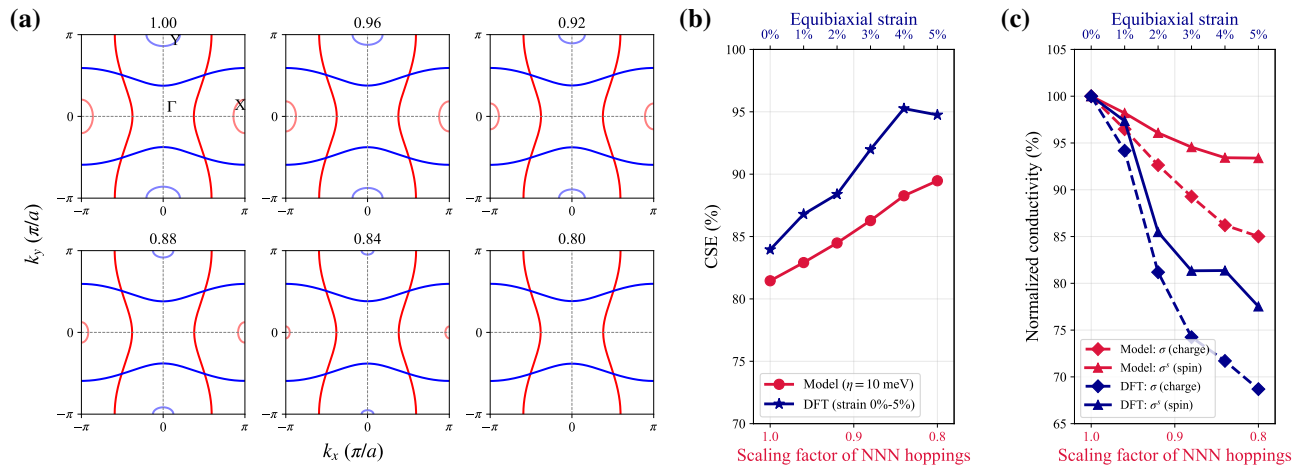


FIG. 4. Strain-induced evolution of the Fermi surface and transport properties in the effective tight-binding model for  $KV_2Se_2O$ . (a) Spin-resolved Fermi surfaces in the  $k_z = 0$  plane as the NNN hopping parameters are uniformly scaled from 1.00 (pristine) to 0.80 in steps of 0.04. Red and blue contours correspond to spin-up and spin-down bands, respectively. (b) CSE evaluated from the Kubo formula with broadening  $\eta = 10$  meV and from DFT results ( $\eta = 10$  meV). The CSE increases monotonically from  $\sim 82\%$  to  $\sim 90\%$  as the pockets are suppressed. (c) Normalized charge conductivity  $\sigma$  and spin conductivity  $\sigma^s$ . Solid and dashed lines represent model and DFT results, respectively.

is a direct consequence of the pockets acting as conductive channels that contribute constructively to the charge current yet destructively to the spin current. Their removal therefore increases the CSE, driving the system toward the ideal flat-band limit. The same trend is consistently observed in the DFT transport data listed in Table I: as the tensile strain increases from 0% to 5%, the spin conductivity  $\sigma^s$  gradually declines while the CSE climbs from  $\sim 84\%$  to  $\sim 95\%$  at 4% strain. This quantitative agreement between the model and DFT results firmly establishes the suppression of parasitic pockets as the primary mechanism for the strain-enhanced charge-to-spin conversion in  $KV_2Se_2O$ . The remaining discrepancy in the maximum CSE ( $\sim 90\%$  vs.  $\sim 96\%$ ) is attributed to the incomplete renormalization of nearest-neighbor hopping anisotropies under the simplified uniform scaling. A detailed discussion of the quantitative differences between the model and the DFT results is provided in the Supplemental Material [20].

**Conclusion**—In summary, we have demonstrated that the CSE in the  $d$ -wave altermagnet  $KV_2Se_2O$  can be systematically enhanced to near the theoretical limit of 100% by in-plane equibiaxial tensile strain. Using effective model analysis and DFT calculations, we established that residual elliptical Fermi pockets near  $X$  and  $Y$ —arising from band warping—act as parasitic channels that dilute the spin conductivity. Strain engineering eliminates these pockets, restoring the ideal orthogonal flat Fermi surfaces and boosting the CSE to a record  $\sim 96\%$  at 4% strain. While Lai *et al.* [14] achieved  $\sim 98\%$  CSE

through electron doping, strain offers a more intrinsic route: it directly manipulates the lattice to restore the flat-band geometry without introducing extrinsic carriers or altering the Fermi level. Chemical doping, in contrast, inevitably introduces disorder and shifts the system away from charge neutrality. Strain is a clean, continuously tunable parameter, readily accessible in epitaxial thin-film platforms and compatible with conventional semiconductor processing [28, 29]. Furthermore, we uncovered an unconventional out-of-plane spin current component  $\sigma_{\uparrow\downarrow}^{\text{n}}$  that achieves a CSE of nearly 55% at optimal orientations, enabling field-free perpendicular magnetization switching. Our findings establish a materials-by-design strategy for maximizing  $\mathcal{T}$ -odd spin currents in altermagnets and position strain-tuned  $KV_2Se_2O$  as a premier platform for next-generation spintronic devices.

**Acknowledgments**—The authors would like to acknowledge the financial support from National Key Research and Development Program of China (Grant No. 2022YFA1602701), and National Natural Science Foundation of China (Grants No. 12574131, No. 12327806, and No. 12227806).

**Data Availability**—The data that support the findings of this article are not publicly available upon publication because it is not technically feasible and/or the cost of preparing, depositing, and hosting the data would be prohibitive within the terms of this research project. The data are available from the authors upon reasonable request.

- [1] L. Šmejkal, R. González-Hernández, T. Jungwirth, and J. Sinova, Crystal time-reversal symmetry breaking and spontaneous Hall effect in collinear antiferromagnets, *Sci. Adv.* **6**, eaaz8809 (2020).
- [2] I. Mazin, Editorial: Altermagnetism—A New Punch Line of Fundamental Magnetism, *Phys. Rev. X* **12**, 040002 (2022).
- [3] L. Šmejkal, J. Sinova, and T. Jungwirth, Beyond Conventional Ferromagnetism and Antiferromagnetism: A Phase with Non-relativistic Spin and Crystal Rotation Symmetry, *Phys. Rev. X* **12**, 031042 (2022).
- [4] L. Šmejkal, J. Sinova, and T. Jungwirth, Emerging Research Landscape of Altermagnetism, *Phys. Rev. X* **12**, 040501 (2022).
- [5] L. Šmejkal, A. H. MacDonald, J. Sinova, S. Nakatsuji, and T. Jungwirth, Anomalous hall antiferromagnets, *Nat. Rev. Mater.* **7**, 482 (2022).
- [6] H.-Y. Ma, M. Hu, N. Li, J. Liu, W. Yao, J.-F. Jia, and J. Liu, Multifunctional antiferromagnetic materials with giant piezomagnetism and noncollinear spin current, *Nat. Commun.* **12**, 2846 (2021).
- [7] J. Krempaský, L. Šmejkal, S. W. D'Souza, M. Hajlaoui, G. Springholz, K. Uhlířová, F. Alarab, P. C. Constantinou, V. Strocov, D. Usanov, W. R. Pudenko, R. González-Hernández, A. Birk Hellenes, Z. Jansa, H. Reichlová, Z. Šobáň, R. D. Gonzalez Betancourt, P. Wadley, J. Sinova, D. Kriegner, J. Minár, J. H. Dil, and T. Jungwirth, Altermagnetic lifting of Kramers spin degeneracy, *Nature* **626**, 517 (2024).
- [8] L. Bai, W. Feng, S. Liu, L. Šmejkal, Y. Mokrousov, and Y. Yao, Altermagnetism: exploring new frontiers in magnetism and spintronics, *Adv. Funct. Mater.* **34**, 2409327 (2024).
- [9] P. Liu, J. Li, J. Han, X. Wan, and Q. Liu, Spin-Group Symmetry in Magnetic Materials with Negligible Spin-Orbit Coupling, *Phys. Rev. X* **12**, 021016 (2022).
- [10] Y. Guo, H. Liu, O. Janson, I. C. Fulga, J. van den Brink, and J. I. Facio, Spin-split collinear antiferromagnets: A large-scale ab-initio study, *Mater. Today Phys.* **32**, 100991 (2023).
- [11] R. González-Hernández, L. Šmejkal, K. Výborný, Y. Yahagi, J. Sinova, T. c. v. Jungwirth, and J. Železný, Efficient electrical spin splitter based on nonrelativistic collinear antiferromagnetism, *Phys. Rev. Lett.* **126**, 127701 (2021).
- [12] H. Bai, Y. C. Zhang, Y. J. Zhou, P. Chen, C. H. Wan, L. Han, W. X. Zhu, S. X. Liang, Y. C. Su, X. F. Han, F. Pan, and C. Song, Efficient Spin-to-Charge Conversion via Altermagnetic Spin Splitting Effect in Antiferromagnet RuO<sub>2</sub>, *Phys. Rev. Lett.* **130**, 216701 (2023).
- [13] C. Song, H. Bai, Z. Zhou, L. Han, H. Reichlova, J. H. Dil, J. Liu, X. Chen, and F. Pan, Altermagnets as a new class of functional materials, *Nat. Rev. Mater.* **10**, 473 (2025).
- [14] J. Lai, T. Yu, P. Liu, L. Liu, G. Xing, X.-Q. Chen, and Y. Sun, *d*-Wave Flat Fermi Surface in Altermagnets Enables Maximum Charge-to-Spin Conversion, *Phys. Rev. Lett.* **135**, 256702 (2025).
- [15] B. Jiang, M. Hu, J. Bai, Z. Song, C. Mu, G. Qu, W. Li, W. Zhu, H. Pi, Z. Wei, Y.-J. Sun, Y. Huang, X. Zheng, Y. Peng, L. He, S. Li, J. Luo, Z. Li, G. Chen, H. Li, H. Weng, and T. Qian, A metallic room-temperature *d*-wave altermagnet, *Nat. Phys.* **21**, 754 (2025).
- [16] J. Wang, W. Zhang, Y. Liu, J. Hu, Z. Zhang, R. Xiong, and Z. Lu, Strain-engineered modulation of non-relativistic altermagnetic spin splitting in rutile RuO<sub>2</sub>, *Mater. Today Phys.* **63**, 102081 (2026).
- [17] Y. Bang, X. Chen, P. Guo, Q. Liu, S. Liu, J. Wang, B. Shen, Y. Han, G. Wang, J. Wang, S. Wang, Z. Zeng, X. Zhang, K. L. Wang, and W. Zhao, Strain-tunable altermagnetism and unconventional topological states in MnTe, *Phys. Rev. B* **109**, 104408 (2024).
- [18] Y. Zhang, J. Liu, J. Ding, Z. Cao, C. Liu, C. Xu, S. Liu, H. Zhang, J. Yu, D. Wu, W. Luo, Q. Liu, K. L. Wang, W. Zhao, and Q. Wang, Tuning spin splitting and anomalous Hall effect in *g*-wave altermagnet CrSb thin films via strain engineering, *Phys. Rev. B* **110**, 094437 (2024).
- [19] W. Zhang, M. Zheng, Y. Liu, Z. Zhang, R. Xiong, and Z. Lu, Strain-induced nonrelativistic altermagnetic spin splitting effect, *Phys. Rev. B* **112**, 024415 (2025).
- [20] See Supplemental Material at [URL will be inserted by publisher] for (I) Computational methods and Kubo formula, (II) Supplementary band structures, (III) Effective model and altermagnetic symmetry, (IV) Rotation of the spin conductivity tensor and angular dependence of the spin currents, (V) Supplementary discussion: Discrepancies between the effective model and DFT transport results.
- [21] P. A. Lee, Localized states in a *d*-wave superconductor, *Phys. Rev. Lett.* **71**, 1887 (1993).
- [22] S. Bhowal and N. A. Spaldin, Ferroically Ordered Magnetic Octupoles in *d*-Wave Altermagnets, *Phys. Rev. X* **14**, 011019 (2024).
- [23] X. Wu, D. Di Sante, T. Schwemmer, W. Hanke, H. Y. Hwang, S. Raghu, and R. Thomale, Robust  $d_{x^2-y^2}$ -wave superconductivity of infinite-layer nickelates, *Phys. Rev. B* **101**, 060504 (2020).
- [24] V. I. Anisimov, J. Zaanen, and O. K. Andersen, Band theory and Mott insulators: Hubbard *U* instead of Stoner *I*, *Phys. Rev. B* **44**, 943 (1991).
- [25] S. L. Dudarev, G. A. Botton, S. Y. Savrasov, C. J. Humphreys, and A. P. Sutton, Electron-energy-loss spectra and the structural stability of nickel oxide: An LSDA+*U* study, *Phys. Rev. B* **57**, 1505 (1998).
- [26] C. K. Majumdar and D. K. Ghosh, On next-nearest-neighbor interaction in linear chain. I, *J. Math. Phys.* **10**, 1388 (1969).
- [27] C. K. Majumdar and D. K. Ghosh, On next-nearest-neighbor interaction in linear chain. II, *J. Math. Phys.* **10**, 1399 (1969).
- [28] G. Zhao, Z. Meng, W. Huang, P. Qin, S. Ruan, L. Ma, L. Zhu, Y. He, L. Liu, Z. Duan, X. Wang, H. Chen, S. Jiang, J. Li, X. Tan, K. Ozawa, B. Wang, J. Cheng, Q. Zhang, J. Wang, C. Chen, and Z. Liu, Pressure-induced metal-insulator and paramagnet-altermagnet transitions in rutile OsO<sub>2</sub> single crystals[J], *Newton* , 100441 (2026).
- [29] H. Jiang, L. Wang, S. Hu, W. Xie, Y. Min, J. Yang, F. Liu, Y. Lu, L. Xie, and H. Huang, Strain-Induced Giant Enhancement of Magnetism in RuO<sub>2</sub> Films[J], *Adv. Funct. Mater.* **n/a**, e28172.